Grain Boundary Chloride Interface Segregation Enhances Conductivity in Hematite without Altering the Band Gap

Cátia A. P. Alves[a*], Andre L. da Silva[a], Vitor L. Martins[b], Bruno Ramos[c] and Douglas Gouvêa[a]

[a] *Department of Metallurgical and Materials Engineering, Escola Politécnica, University of São Paulo, São Paulo, 05508-010, Brazil*

[b] *Departamento de Química Fundamental, Instituto de Química, Universidade de São Paulo, Av. Prof. Lineu Prestes 748, CEP 05508-000, São Paulo, SP, Brazil*

c Microfluidic & Photoelectrocatalytic Engineering Lab. Department of Chemical Engineering, Centro Universitário FEI, São Bernardo do Campo, SP, Brazil

*E-mail:catia.alves@usp.br

ABSTRACT

Nanocrystalline Fe_2O_3 with controlled chloride additions was used to evaluate how interfacial Cl segregation governs grain-boundary electrical transport. XRF quantified the retained chloride, while selective surface lixiviation and interface-excess analysis separated surface from grain-boundary (GB) contributions, revealing preferential segregation at GBs. X-ray diffraction showed hematite with modest crystallite-size changes. UV-Vis reflectance spectroscopy indicated an almost invariant optical band gap (~2.18 eV), whereas the color difference increased with retained Cl^-, consistent with defect/surface states. Room-temperature impedance spectroscopy resolved bulk and GB responses and showed a marked drop in resistivity with increasing Cl^-; after lixiviation, conductivity partially decreased, confirming the interfacial origin. The rise in conductivity surpasses a simple carrier-count model ($\sigma \propto N$), implicating mobility enhancement via GB-barrier lowering. Interfacial chloride segregation thus offers a practical route to increase the electrical conductivity of polycrystalline Fe_2O_3 without altering its band structure, advancing interface-engineered routes for electronic and photoelectrochemical applications.

Keywords: hematite (α-Fe_2O_3); chloride doping; interfacial segregation; grain-boundary transport; impedance spectroscopy.

1. Introduction

Iron oxide (Fe_2O_3) nanoparticles are central to applications in catalysis, energy conversion, and sensing [1-7], yet their performance is often limited by short carrier lifetimes, low diffusion length, and intrinsically low electrical conductivity [8]. Interface engineering, via interfacial segregation quantified by surface/grain boundary interface excess and assisted by selective lixiviation, has emerged as an effective route to mitigate these bottlenecks [9-11].

A key pathway is interfacial segregation of dopants, which redistributes species between surfaces and grain boundaries (GBs) and can lower the electrostatic barrier that blocks charge transport across GBs [12-15]. This concept has improved stability and transport in several oxides via quantified interface excess and targeted segregation, and recently been demonstrated to tune grain-boundary conductivity in related ceramics [16]. Notably, anion doping (e.g., halides) has been shown to enhance conductivity in polycrystalline semiconductors by decreasing the GB barrier [10]. However, for hematite, the role of chloride segregation, its partition between surface and GBs, its persistence after selective lixiviation, and its direct impact on electrical transport, has not been systematically established or quantitatively connected to optical and impedance responses.

Here we test the hypothesis that retained chloride segregated at grain boundaries is the primary driver for the conductivity enhancement in nanocrystalline Fe_2O_3, without measurably altering the bulk band gap. We synthesize Fe_2O_3 with controlled chloride additions, quantify the retained Cl^- by X-ray fluorescence (XRF), and use selective lixiviation to separate surface from GB contributions [8]. The interface excess of Cl^- at surfaces (Γ_s) and GBs (Γ_{gb}) is determined and related to its bandgap energy (E_g) and room-temperature resistivity. Finally, we benchmark the conductivity increase against a carrier-count model ($\sigma \propto N$) to demonstrate that the observed gains exceed what carrier density alone can explain, implicating mobility enhancement via GB-barrier lowering. This establishes interfacial Cl^- segregation as a practical lever to improve the electrical performance of polycrystalline Fe_2O_3 while preserving its fundamental band structure.

2.Materials and methods

2.1. Synthesis of Cl-doped Fe_2O_3 nanopowders

Fe_2O_3 nanopowders were synthesized by the polymeric precursor method [17]. The synthesis used 45.8 wt % anhydrous citric acid (Synth, $C_6H_8O_7$, ≥ 99.00 wt % purity), 30.5 wt % ethylene glycol (Synth, $C_2H_6O_2$, ≥ 99.00 wt % purity), and 23.6 wt % hydrated iron nitrate (Synth, Fe $(NO_3)_3$, ≥ 99.98 wt % purity) as the iron source. Chloride was introduced by adding calculated amounts of NH_4Cl (Synth, ≥ 99.5 wt % purity) aqueous solution to the resin. The target molar concentrations of Cl^- were x= 0.0, 0.1, 0.5, 1.0, 5.0, and 10.0 %. However, the molar concentrations of Cl^- obtained after calcination were x= 0.0, 0.03, 0.04, 0.05, 0.18 and 0.23%. The lower amount of Cl^- was probably due to evaporation losses during calcination. The Cl-doped samples were labeled as FeCl-x, and the undoped sample was labeled as Fe_2O_3. Calcination was carried out under air flow at 300 °C for 10 h in a muffle furnace.

2.2. Powder characterization

Chemical compositions were determined by XRF using a Malvern Panalytical spectrometer model Zetium. The X-ray diffraction (XRD) patterns were obtained using an X'Pert-MPD (Philips) diffractometer with Cu Kα radiation, operated at 45 kV and 40 mA. The step size was set at 0.02° 2θ per second over the 5-90° 2θ range. The crystallite sizes and the lattice parameters were calculated by Rietveld refinement using the X'Pert Highscore software, with $MgAl_2O_4$ as the standard. Powder density was measured with a Micromeritics AccuPyc II 1340 He gas pycnometer after 200 purges for degassing. Specific surface areas were determined by nitrogen adsorption at 77 K (Micromeritics Gemini III 2375), according to the Brunauer-Emmett-Teller (BET) method. Samples were degassed at 250 °C for ~12 h before the experiment using a VacPrep 061 (Micromeritics).

2.3. Surface characterization

The selective lixiviation method was employed to determine the Cl^- surface excess [8]. Approximately 200 mg of powder was sonicated with ~1.8 g of distilled water for 1 h. The matrix, *i.e.*, Fe_2O_3, which is insoluble in distilled water, was then separated from the supernatant by centrifuging three times for 30 minutes at 13,000 rpm. Approximately 1 g of the supernatant was collected, diluted in ~5 g of distilled water, and analyzed using a chlorine selective electrode (Hanna Instruments).

Diffuse reflectance infrared Fourier transform (DRIFT) spectroscopy was performed using a Nicolet iS50 spectrometer to identify the functional groups adsorbed on the powder. DRIFT spectra were recorded in the range of 400-4000 cm^{-1}. Transmission Electron Microscopy (TEM) images of Fe_2O_3 nanoparticles were obtained using a Titan Themis Cubed (FEI Company) microscope equipped with double aberration correction and operated at 300 kV.

2.4. Optical and electrical characterizations

UV-vis spectra were investigated using a Shimadzu UV-2600 spectrometer equipped with an integrating sphere to record the diffuse reflectance spectra (DRS) of the samples.

The color of the undoped Fe_2O_3 and Cl-doped Fe_2O_3 samples, both nonlixiviated and lixiviated, was evaluated using a MiniScan XE Plus colorimeter (HunterLab). Measurements were carried out according to the CIE Lab* color space standard (CIE 1976) [18], employing standard daylight (D65) as the illuminant and a 10° standard observer. The instrument was calibrated using white and black reference tiles supplied by the manufacturer.

Impedance spectroscopy (IS) measurements were carried out using a Gamry reference 600+ potentiostat/galvanostat. Samples were prepared by dry pressing using a uniaxial press at 294 MPa. Cylindrical pellets with 11 mm diameter and 1.5 mm thickness were used in the experiments. Thermal treatment was performed at 325 °C for 2 h to enhance the grain boundary area and enable electrical measurements. Low-temperature-curing silver ink was used to deposit contact pads on the parallel surfaces of the pellets. Samples were dried at 80 ºC under vacuum overnight before being assembled between two stainless-steel current collectors in a 12 mm diameter Swagelok union-type cell inside an Ar-filled glovebox (moisture and oxygen content below 2 ppm). IS data was collected in the frequency range of 1 MHz to 0.01 Hz with 100 mV AC voltage amplitude at room temperature, within a Faraday cage (Gamry). The obtained spectra were fitted using Z-View 4.0 software.

3. Results and Discussions

3.1. Powder characterizations

The X-ray diffraction patterns for undoped Fe_2O_3 and Cl-doped Fe_2O_3 samples are shown in

Figure *1*. Broad peaks are observed, which is typical of nanosized crystallites. Hematite (JCPDS card no. 24-0072) was identified as the main phase. A secondary maghemite phase was detected only in the FeCl-0.18 sample, which is likely an effect of Cl^- doping.

The average crystallite sizes and lattice parameters are shown in Table 1. The crystallite size of the undoped Fe_2O_3 sample is consistent with the literature [19]. However, a slight increase was observed in the doped samples up to 0.05 mol% Cl^-, possibly due to changes in diffusion parameters caused by Cl^- segregation at interfaces [20]. At low doping levels, diffusion dominates, whereas at higher dopant contents interface segregation induces the decrease in crystallite size. This decrease, observed for the FeCl-0.18 and FeCl-0.23 samples, may be related to a balance in interfacial energy due to segregation. Similar behavior has been reported for Sb-doped TiO_2 [21] and ZnO-doped SnO_2 [22]. These two contributions to crystallite size evolution, diffusion and surface energy, are more clearly illustrated by Eq. (1) [23, 24].

$$d_t^n - d_0^n = kD\gamma_i t \qquad (1)$$

where, d_0 is the average particle size at t_0; D is the diffusion coefficient; γ_i is the interfacial energy; k is a constant that depends on the kinetic model; and n (typically 2, 3, or another integer) indicates the grain-growth mechanism [9].

Consistent with the behavior of FeCl-0.18 and FeCl-0.23, segregation lowers γ_i and, therefore, the growth rate predicted by Eq. (1). Consequently, reductions in interfacial energy, arising from changes in the interfacial chemical and from the build-up of interfacial excess (see Eqs. (1) and (2)), stabilize nanoparticles and inhibit grain-growth. This decrease in γ_i slows grain-growth kinetics [23, 24]. This nanoparticle stabilization is significant: the relative amount of segregation at grain boundaries versus surfaces governs the stability of these interfaces [24].

$$\gamma_i = \gamma_{i0} + \Gamma_i \Delta H_{seg} \qquad \text{where } \Gamma_i = \frac{n}{A_i} \text{ and } \Delta H_{seg} < 0 \qquad (2)$$

The lattice parameters of Fe_2O_3 were consistent with the literature [25, 26] and showed no significant changes upon Cl^- doping.

	Hematite				**Maghemite**		
Sample	Lattice parameters a=(b) (Å)	Lattice parameters c (Å)	Crystallite size (nm)	Phase fraction (wt%)	Lattice parameters a (Å)	Crystallite size (nm)	Phase fraction (wt%)
Fe_2O_3	5.0377(5)	13.761(2)	37.57±0.78	100	-	-	-
FeCl-0.03	5.0377(5)	13.760(2)	39.52±0.73	100	-	-	-
FeCl-0.04	5.0376(4)	13.760(1)	46.57±1.07	100	-	-	-
FeCl-0.05	5.0372(4)	13.759(1)	46.88±1.22	100	-	-	-
FeCl-0.18	5.0368(4)	13.757(1)	41.20±0.85	86.6	8.353 (2)	27.14±2.49	13.4
FeCl-0.23	5.0381(4)	13.761(2)	40.22±0.88	100	-	-	-

Density, specific surface area (SSA), total specific area (TSA), specific grain-boundary (SGB) area, and SGB/SSA ratio are listed in Table 2. TSA was calculated using Eq. (3), assuming a truncated-octahedron crystallite shape, where *d* is the average crystallite size and ρ is the measured density [27]. The SGB area, defined as half the difference between TSA and SSA, was calculated using Eq. (4).

$$TSA = \frac{7.11}{d.\rho} \qquad (3)$$

$$SGB = \frac{(TSA - SSA)}{2} \qquad (4)$$

The measured density decreased with increasing Cl^- content. This trend can be attributed to the formation of point defects, such as iron vacancies, generated to maintain electroneutrality when O^{2-} is replaced by Cl^- in the lattice [28].

Sample	Density (g/cm^3)	SSA (m^2/g)	TSA (m^2/g)	SGB (m^2/g)	SGB/SSA ratio
Fe_2O_3	4.99±0.02	14.01±0.07	37.90±0.02	11.95±0.09	0.86±0.01
FeCl-0.03	4.99±0.01	13.89±0.03	35.99±0.02	11.10±0.08	0.80±0.01
FeCl-0.04	4.97±0.02	15.12±0.09	30.67±0.02	7.78±0.05	0.53±0.01
FeCl-0.05	4.97±0.02	14.09±0.09	30.49±0.03	8.20±0.06	0.56±0.01
FeCl-0.18	4.82±0.02	23.11±0.08	35.75±0.03	6.32±0.03	0.26±0.01
FeCl-0.23	4.83±0.03	27.74±0.16	36.55±0.02	4.40±0.02	0.14±0.01

At low additive levels (0.03-0.05 mol%), the SSA showed no significant change. By contrast, the FeCl-0.18 and FeCl-0.23 samples exhibited a slight increase in SSA. This trend is consistent with a balance in interfacial energy driven by interfacial segregation and is better interpreted together with SGB and the SGB/SSA ratio. For the Cl-doped Fe_2O_3 samples, both SGB and the SGB/SSA decreased, indicating that the dopant stabilizes surfaces more than grain boundaries, which also explains the higher SSA observed for FeCl-0.18 and FeCl-0.23. TSA decreased up to 0.05 mol% and then increased for FeCl-0.18 and FeCl-0.23 samples.

3.2. Interfacial segregation

For a better understanding of the effects of Cl^- doping in Fe_2O_3, it is important to quantify the dopant distribution at interfaces. The amount segregated at the nanoparticle surfaces was quantified directly by the selective lixiviation method, whereas dopant segregated at GBs or dissolved in the bulk was estimated. From the crystallite-size trend, the increase in particle size up to 0.05 mol% Cl^- is likely associated with the bulk solubility of Cl^- in Fe_2O_3 nanoparticles. Accordingly, in this study we considered the bulk solubility of Cl^- to be ~0.05 mol%. This estimate is consistent with the large differences between O^{2-} and Cl^- in ionic charge and radius, indicating low Cl^- solubility in the Fe_2O_3 matrix.

Interfacial excess (Γ) was determined by selective lixiviation. First, the number of moles of Cl^- segregated at the grain boundaries (n_{gb}) was obtained as the difference between the total Cl^- content (n_T) and the amounts dissolved in the bulk (n_{bulk}) and segregated at the surface (n_S)as in Eq. (5) [23]:

$$n_{gb} = n_T - n_{bulk} - n_S \qquad (5)$$

Then, the grain-boundary excess (Γ_{gb}) was calculated using Eq. (6) [23]:

$$\Gamma_{gb} = \frac{n_{gb}}{SGB} \qquad (6)$$

The surface and grain-boundary excesses (Γ_S *and* Γ_{gb}) are summarized in **Error! Reference source not found.**.

Sample	Γ_S (µmol/m^2)	Γ_{gb} (µmol/m^2)
Fe_2O_3	0.095±0.001	5.98±0.04
FeCl-0.03	0.179±0.001	5.98±0.06
FeCl-0.04	0.387±0.004	7.10±0.07
FeCl-0.05	0.651±0.005	9.40±0.08
FeCl-0.18	1.523±0.008	20.52±0.11
FeCl-0.23	1.973±0.013	21.45±0.14

Table 3 shows that most of the Cl^- segregated at the GBs rather than at particle surfaces. The trace Cl^- detected in the undoped Fe_2O_3 sample most likely originated from precursor impurities in the Pechini method. This distribution is relevant because GB segregation is expected to lower the grain-boundary potential-barrier height for charge transport, thereby increasing the overall electrical conductivity of the system [10].

3.3. DRIFTS and TEM

DRIFTS and TEM were carried out on undoped and Cl-doped Fe_2O_3, in both lixiviated and nonlixiviated samples. The aim was to measure the effects of doping and of the selective lixiviation process.

Figure 2a–c show the DRIFTS spectra of undoped and Cl-doped Fe_2O_3 before and after lixiviation. All spectra displayed well-defined bands assigned to adsorbed H_2O (3500-3200 cm^{-1}) [29], hydroxyl groups (~3680 and 1630 cm^{-1}) [29], adsorbed CO_2 (2330 cm^{-1}), adsorbed carbonate (CO_3^{2-}, 1540-1290 cm^{-1}) and Fe-O bands (1000-400 cm^{-1}) [30, 31]. The features due to adsorbed H_2O, CO_2, and carbonate did not change upon lixiviation in any of the samples. Changes were observed only in the Fe-O region, particularly the Fe-OOH band, which can be attributed to the surface hydration during the selective lixiviation process.

The morphology and microstructure of the synthesized Fe_2O_3 samples were further characterized using TEM and high-resolution TEM (HRTEM). Figures 3a, 3c, and 3e present TEM micrographs of Fe_2O_3, FeCl-0.23, and lixiviated FeCl-0.23, respectively.

The nanoparticles did not show any visible differences between the undoped and Cl-doped Fe_2O_3 samples. The same was observed for nonlixiviated and lixiviated samples (Figure 3c, e). These representative TEM micrographs show agglomerated nanoparticles forming elongated aggregates. Due to this irregular morphology and agglomeration, a reliable particle-size distribution could not be determined; nevertheless, spot measurements yielded particle sizes comparable to the crystallite size obtained from XRD. HRTEM lattice fringes confirmed well-crystallized Fe_2O_3 with a spacing of 0.37 nm, indexed to the (012) plane of hematite.

3.4. Optical and electrical characterizations

Figure 4 shows the UV-Vis diffuse reflectance spectra of undoped and Cl-doped Fe_2O_3. All samples exhibited a prominent reflectance peak in the 1.6-2.0 eV region, characteristic of hematite electronic transitions [32]. Increasing Cl^- content led to a progressive decrease in peak intensity, most pronounced for FeCl-0.18 and FeCl-0.23, consistent with enhanced absorption in the visible range. Above ~2.2 eV the reflectance remained low for all compositions, with only minor variations among doping levels. These trends are consistent with variations in defect/surface states rather than with a modification of the bulk band structure, in agreement with the nearly constant band gap obtained from Tauc plots (Figure 5). The optical band gap (E_g) was then determined using the Tauc model [33], according to the Eq. (7):

$$(\alpha \cdot h\upsilon)^{\frac{1}{\beta}} = B(h\upsilon - E_g) \qquad (7)$$

where α is the absorption coefficient dependent on photon energy, *h* is Planck's constant, *v* is the frequency of the incident radiation, and *B* is a material-dependent constant. The value of *β* depends on the type of electronic transition, being 0.5 for direct transitions and 2 for indirect transitions. α-Fe_2O_3 exhibits indirect electronic transitions [34]; therefore, *β* = 2 was adopted in Eq. (7) to determine the band gap energy.

To estimate *α*, the Kubelka–Munk function [35] was used, as given by Eq. (8), where R_∞ represents the ratio between the reflectance of the sample and that of the standard:

$$\alpha \approx F(R) = \frac{(1-R_\infty)^2}{2R_\infty} \qquad (8)$$

Substituting Eq. (8) into Eq. (7) yields the following relationship, which was used to estimate the band gap energy:

$$((F(R) \cdot h\upsilon)^{\frac{1}{2}} = B(h\upsilon - E_g) \qquad (9)$$

Figure 5 presents the corresponding Tauc plots for undoped and Cl-doped Fe_2O_3, from which E_g values were extracted.

The direct extrapolation of the linear region yields an optical band gap (E_g) of ~2.16 ± 0.01 eV for all compositions. Thus, at the investigated concentrations, Cl^- does not measurably change the fundamental band gap of hematite. The invariance of E_g

indicates that chloride primarily influences the optical response through defect/surface states, rather than by shifting the bulk band edges. Consistent with this interpretation, the UV-vis reflectance shows a marked reduction in the 1.6–2.0 eV range (i.e., enhanced absorption), particularly for FeCl–0.18 and FeCl–0.23.

Figure *6* presents the color difference ΔE*ab (CIE76) for undoped and Cl-doped Fe_2O_3, referenced to the undoped sample under the same condition (nonlixiviated or lixiviated), as a function of the retained Cl^- content measured by XRF. ΔE was calculated using Eq. (10). The individual L*, a*, and b* trends for each composition (before and after lixiviation) are provided in the Supplementary Information (Figure 1S).

$$\Delta E = [(\Delta L *)^2 + (\Delta a *)^2 + (\Delta b *)^2]^{1/2} \qquad (10)$$

ΔE^*_{ab} (CIE76) increases with the amount of retained Cl^- for both series, reaching visibly distinct colors at higher contents; in the lixiviated series, a maximum is observed near ~0.18 mol% and slightly declines at the highest composition. These trends indicate that the perceived color is governed by the fraction of chloride effectively incorporated and/or by defect states left after lixiviation, rather than by the nominal Cl^- added to the sample. Consistently, the individual **a*** and **b*** coordinates show a net decrease with increasing Cl (loss of red and yellow components), whereas **L*** varies less markedly; the full **L*, a*, b*** evolutions before and after lixiviation are provided in the Supplementary Information (Figure 1S).

Guided by interfacial Cl^- segregation (Table 3), invariant Eg (Figure 5), and ΔE^*_{ab} scaling with retained Cl^- (Figure 6), we hypothesize that chloride primarily affects grain-boundary transport by lowering the interfacial barrier. To test this scenario, room-temperature impedance spectra were acquired for undoped and Cl-doped Fe_2O_3 before (nonlixiviated) and after lixiviation (Figure 7a, b). All samples exhibited similar porosities (~50.0 ± 8.0 vol%) and were carefully prepared under identical experimental conditions to minimize contributions from adsorbed species within the porous network. This comparability allows differences in the IS response to be attributed primarily to changes in the electrical microstructure (bulk vs. grain boundary), rather than to morphological artifacts.

The total electrical resistivity (ρ) of the undoped Fe_2O_3 pellet was 5.8 x 10^8 Ω.m and increased to 8.5 x 10^8 Ω.m after lixiviation. Previous reports showed that α-Fe_2O_3 exhibits a resistivity of 2 x 10^6 Ω.m at 27 °C [36], however, the authors did not report the sample porosity.

All undoped and Cl-doped Fe_2O_3 samples exhibited two depressed semicircles and were fitted with a series of R-CPE elements; in polycrystalline oxides, the higher-frequency arc with lower capacitance is assigned to the bulk, whereas the lower-frequency arc with higher capacitance corresponds to the grain boundary, in line with the brick-layer description for electroceramics [37]. Any very-low-frequency contribution, when present, is typically associated with electrode polarization. The total resistivity equals the sum of the fitted resistive terms ($R_1 + R_2$), i.e., the difference between high- and low-frequency Z' intercepts normalized by geometry.

With increasing Cl^- content, ρ decreases markedly for both series and partially recovers after lixiviation, a trend consistent with grain-boundary barrier lowering driven by interfacial chloride segregation. Similar behavior has been reported for Sn- and Zn-doped hematite [12, 13], and analogous conductivity enhancements are observed in Cl-doped ZnO nanoparticles processed under comparable conditions [8, 10]. As a reference, undoped hematite is highly resistive at room temperature, and interface engineering by dopants can shift its conductivity over several orders of magnitude [38].

Figure 8 compiles the electrical conductivity (σ), calculated as $\sigma=1/\rho$, with ρ obtained from the total fitted resistance (R_1+R_2) and the sample geometry ($\rho=R\,A/L$) from the room-temperature IS data, as a function of the retained Cl^- content (XRF). Figure 8a compares nonlixiviated and lixiviated pellets on common axes; Figure 8b shows the relative increase (σ/σ_0) together with the one-electron-per-Cl^- carrier-count model ($\sigma \propto$ N), where σ_0 refers to the undoped sample under the same condition.

From the combination of the lixiviation results and the conductivity trends in Figure 8a, two distinct contributions to the conductivity enhancement can be identified. The first is the ionic conduction provided by Cl^- species segregated at the surface of Fe_2O_3, which strongly increases σ in the non-lixiviated pellets. Once these surface ions are removed by lixiviation, the conductivity drops sharply, revealing the second contribution: the electronic conduction facilitated by Cl^- remaining at grain boundaries, which lowers the grain-boundary barrier and thus sustains part of the conductivity. The reduced σ of the lixiviated samples therefore directly reflects the loss of the surface ionic pathway, while the residual conductivity is governed primarily by the grain-boundary electronic mechanism.

Figure 8b benchmarks the conductivity gain against a simple carrier-count model derived from Eq. (10)

$$\sigma = N\mu|e| \qquad (10)$$

If each Cl^- contributed one electron and μ remained constant, the relative increase in σ should track the relative increase in N (taken as proportional to the retained Cl^-). Instead, the measured rise in σ far exceeds the change expected from N alone—most notably at higher Cl^- contents, indicating that the enhancement cannot be explained exclusively by carrier concentration. Put differently, to match the observed σ using Eq.

(10) with a bulk-only picture would require effective carrier densities tens to hundreds of times larger than those provided by the nominal Cl^- (as sketched by the "N" curve), which is unrealistic. We therefore infer a dominant increase in carrier mobility, consistent with grain-boundary barrier lowering driven by interfacial chloride; the partial reduction of σ after lixiviation further supports this interfacial mechanism [39].

4. Conclusions

This work shows that chloride introduced by the polymeric-precursor route modulates the interfacial chemistry of nanocrystalline Fe_2O_3, driving preferential segregation at grain boundaries ($\Gamma_{\mathrm{gb}} > \Gamma_{\mathrm{S}}$). Selective lixiviation combined with interface-excess analysis separates surface and GB contributions, while XRD confirms hematite as the main phase with modest crystallite-size changes governed by the balance between diffusion and the reduction of interfacial energy induced by segregation.

Optically, UV-vis DRS reveals an essentially invariant optical band gap (~2.18 eV); the color difference ΔE_{ab}^{*} increases with retained Cl^-, consistent with changes in defect/surface states rather than band-edge shifts. Room-temperature impedance spectroscopy resolves bulk and GB arcs and shows a marked drop in total resistivity with increasing Cl^-; after lixiviation, the conductivity partially declines, confirming the interfacial origin of the effect. Moreover, the conductivity gain exceeds a simple carrier-count expectation ($\sigma \propto N$), indicating mobility enhancement via GB-barrier lowering rather than a bulk doping effect.

Altogether, the data demonstrate that the conductivity improvement in Cl-modified Fe_2O_3 is predominantly governed by grain-boundary processes, achieved without altering the band structure. Interfacial Cl^- segregation therefore emerges as a practical route to tailor the electrical response of polycrystalline Fe_2O_3, with direct relevance to electronic and photoelectrochemical applications.

- ACKNOWLEDGMENTS

We gratefully acknowledge the support of the RCGI – Research Centre for Gas Innovation, hosted by the University of São Paulo (USP) and sponsored by FAPESP – São Paulo Research Foundation (2014/50279-4, 2019/10109-6, and 2017/11937-4) and Shell Brazil, and the strategic importance of the support given by ANP (Brazilian National Oil, Natural Gas, and Biofuels Agency) through the R&D levy regulation. DG is fellow of the Brazilian CNPq. This study was also financed in part by the Coordenação de Aperfeiçoamento de Pessoal de Nível Superior - Brasil (CAPES) - Finance Code 88887.672867/2022-00. VLM thanks FAPESP (2019/26309-4) for financial support. This research was also supported by LNNano – Brazilian Nanotechnology National Laboratory, CNPEM/MCTIC, TEM proposal n. 20230767.

References

[1] Y. Yang *et al.*, "Iron oxide nanoparticle-based nanocomposites in biomedical application," *Trends Biotechnol*, Jul 4 2023.

[2] A. A. B. Kadhim Q. Jabbar, Samir M. Hamad, "Iron oxide nanoparticles: Preparation methods, functions, adsorption and coagulation/flocculation in wastewater treatment " *Environmental Nanotechnology, Monitoring & Management*, vol. 17, 2022.

[3] S. A. C. Carabineiro, N. Bogdanchikova, P. B. Tavares, and J. L. Figueiredo, "Nanostructured iron oxide catalysts with gold for the oxidation of carbon monoxide," *RSC Advances*, vol. 2, no. 7, 2012.

[4] S. P. Raja Selvaraj, Ramesh Vinayagam, Thivaharan Varadavenkatesan, and P. A. D. Ponnusamy Senthil Kumar, Gayathri Rangasamy "A recent update on green synthesized iron and iron oxide nanoparticles for environmental applications," vol. 308, 2022.

[5] P. Sangaiya and R. Jayaprakash, "A Review on Iron Oxide Nanoparticles and Their Biomedical Applications," *Journal of Superconductivity and Novel Magnetism,* vol. 31, no. 11, pp. 3397-3413, 2018.

[6] X. Zheng and J. Li, "A review of research on hematite as anode material for lithium-ion batteries," *Ionics,* vol. 20, no. 12, pp. 1651-1663, 2014.

[7] C. A. Podence Alves, P. H. Palharim, B. Pratto, A. L. da Silva, D. Gouvêa, and B. Ramos, "Photocatalytic ammonia synthesis from nitrogen in water using iron oxides: Comparative efficiency of goethite, magnetite, and hematite," *Journal of Photochemistry and Photobiology A: Chemistry,* vol. 460, p. 116159, 2025/03/01/ 2025.

[8] G. M. Fortes *et al.*, "Cl-Doped ZnO Nanoparticles with Enhanced Photocatalytic Activity via Selective Surface Lixiviation: Implications for Acetaminophen Degradation," *ACS Applied Nano Materials,* vol. 8, no. 5, pp. 2481-2492, 2025.

[9] A. L. da Silva *et al.*, "TiO2 Surface Engineering to Improve Nanostability: The Role of Interface Segregation," *The Journal of Physical Chemistry C,* vol. 123, no. 8, pp. 4949-4960, 2019.

[10] G. M. Fortes, A. L. da Silva, L. B. Caliman, F. C. Fonseca, and D. Gouvêa, "Interfacial segregation in Cl−-doped nano-ZnO polycrystalline semiconductors and its effect on electrical properties," *Ceramics International,* vol. 47, no. 17, pp. 24860-24867, 2021.

[11] A. L. da Silva, J. Bettini, A. A. Bernardes, R. H. R. Castro, and D. Gouvêa, "Improving TiO2 Anatase Nanostability Via Interface Segregation: The Role of the Ionic Radius," *The Journal of Physical Chemistry C*, vol. 127, no. 3, pp. 1536-1547, 2023.

[12] M. R. S. Soares *et al.*, "Unraveling the Role of Sn Segregation in the Electronic Transport of Polycrystalline Hematite: Raising the Electronic Conductivity by Lowering the Grain-Boundary Blocking Effect," *Advanced Electronic Materials*, vol. 5, no. 6, 2019.

[13] M. V. Nikolic *et al.*, "Study of dielectric behavior and electrical properties of hematite α-Fe2O3 doped with Zn," *Science of Sintering*, vol. 44, no. 3, pp. 307-321, 2012.

[14] G. Carraro, A. Gasparotto, C. Maccato, and D. Barreca, "Fluorine-Doped Iron Oxide Nanomaterials by Plasma Enhanced-CVD: An XPS Study," *Surface Science Spectra*, vol. 20, no. 1, pp. 9-16, 2013.

[15] Y. Zhu, J. Xu, H. Jiang, D. Niu, X. Zhang, and S. Hu, "The effect of fluorine doping on the photocatalytic properties of hematite for water splitting," *CrystEngComm*, vol. 20, no. 41, pp. 6430-6437, 2018.

[16] M. Kindelmann *et al.*, "Controlling Grain Boundary Segregation to Tune the Conductivity of Ceramic Proton Conductors," *Advanced Energy Materials*, vol. 15, no. 9, 2024.

[17] P. A. Lessing, "Mixed-cation oxide powders via polymeric precursors," *American Ceramic Society*, vol. 68, pp. 1002-1007, 1989.

[18] J. Schanda, "CIE Colorimetry," in *Colorimetry*, 2007, pp. 25-78.

[19] M. Krispin, A. Ullrich, and S. Horn, "Crystal structure of iron-oxide nanoparticles synthesized from ferritin," *Journal of Nanoparticle Research*, vol. 14, no. 2, 2012.

[20] R. A. M. P. de Oliveira, A. L. da Silva, L. B. Caliman, and D. Gouvêa, "Interface excess on Li2O-doped γ-Al2O3 nanoparticles," *Ceramics International*, vol. 46, no. 8, pp. 10555-10560, 2020.

[21] H. Gandelman, A. L. da Silva, L. B. Caliman, and D. Gouvêa, "Surface and grain boundary excess of ZnO-doped TiO2 anatase nanopowders," *Ceramics International*, vol. 44, no. 10, pp. 11390-11396, 2018.

[22] D. Gouvêa, D. C. C. do Rosário, and L. B. Caliman, "Surface and grain-boundary excess of ZnO-doped SnO2 nanopowders by the selective lixiviation method," *Journal of the American Ceramic Society*, vol. 100, no. 9, pp. 4331-4340, 2017.

[23] R. H. R. Castro, D. Gouvêa, and F. Wakai, "Sintering and Nanostability: The Thermodynamic Perspective," *Journal of the American Ceramic Society*, vol. 99, no. 4, pp. 1105-1121, 2016.

[24] R. H. R. Castro, "On the thermodynamic stability of nanocrystalline ceramics," *Materials Letters*, vol. 96, pp. 45-56, 2013.

[25] M. Mishra and D.-M. Chun, "α-Fe 2 O 3 as a photocatalytic material: A review," *Applied Catalysis A: General*, vol. 498, pp. 126-141, 2015.

[26] A. Cervellino, R. Frison, G. Cernuto, A. Guagliardi, and N. Masciocchi, "Lattice parameters and site occupancy factors of magnetite–maghemite core–shell nanoparticles. A critical study," *Journal of Applied Crystallography*, vol. 47, no. 5, pp. 1755-1761, 2014.

[27] C.-H. Chang, S. Dey, and R. H. R. Castro, "Energetics of Oriented Attachment of Mn-Doped SnO2 Nanoparticles," *The Journal of Physical Chemistry C,* vol. 119, no. 35, pp. 20662-20672, 2015.

[28] R. da Silva Alvim, F. N. Ribeiro, and G. M. Dalpian, "Iron and oxygen vacancies at the hematite surface: pristine case and with a chlorine adatom," *Phys Chem Chem Phys,* vol. 22, no. 43, pp. 25380-25389, Nov 21 2020.

[29] I. M. McIntosh, A. R. L. Nichols, K. Tani, and E. W. Llewellin, "Accounting for the species-dependence of the 3500 cm−1H2Otinfrared molar absorptivity coefficient: Implications for hydrated volcanic glasses," *American Mineralogist,* vol. 102, no. 8, pp. 1677-1689, 2017.

[30] H. Namduri and S. Nasrazadani, "Quantitative analysis of iron oxides using Fourier transform infrared spectrophotometry," *Corrosion Science,* vol. 50, no. 9, pp. 2493-2497, 2008.

[31] L. Mei, L. Liao, Z. Wang, and C. Xu, "Interactions between Phosphoric/Tannic Acid and Different Forms of FeOOH," *Advances in Materials Science and Engineering,* vol. 2015, pp. 1-10, 2015.

[32] J. Li and D. Chu, "Energy band engineering of metal oxide for enhanced visible light absorption," in *Multifunctional Photocatalytic Materials for Energy*, 2018, pp. 49-78.

[33] J. Tauc, "Optical properties and electronic structure of amorphous Ge and Si," *Materials Research Bulletin,* vol. 3, no. 1, pp. 37-46, 1968/01/01/ 1968.

[34] M. F. Al-Kuhaili, M. Saleem, and S. M. A. Durrani, "Optical properties of iron oxide (α-Fe2O3) thin films deposited by the reactive evaporation of iron," *Journal of Alloys and Compounds,* vol. 521, pp. 178-182, 2012.

[35] P. Kubelka, "New Contributions to the Optics of Intensely Light-Scattering Materials. Part I," *Journal of the Optical Society of America*, vol. 38, no. 5, pp. 448-457, 1948/05/01 1948.

[36] G. J. P. N. Guskos, V. Likodimos, S. Patapis, D. Yarmis, A. Przepiera, K. Przepiera, J. Majszczyk, J. Typek, M. Wabia, K. Aidinis, Z. Drazek, "Photoacoustic, EPR and electrical conductivity investigations of three synthetic mineral pigments: Hematite, goethite and magnetite," *Materials Research Bulletin,* vol. 37, pp. 1051-1061, 2002.

[37] J. T. S. I. D. C. Sinclair; and a. A. R. West, "Electroceramics : Characterization by Impedance Spectroscopy," *Advanced Materials*1990.

[38] J. A. Glasscock, P. R. F. Barnes, I. C. Plumb, A. Bendavid, and P. J. Martin, "Structural, optical and electrical properties of undoped polycrystalline hematite thin films produced using filtered arc deposition," *Thin Solid Films,* vol. 516, no. 8, pp. 1716-1724, 2008.

[39] A. Jiamprasertboon *et al.*, "Photocatalytic and electrically conductive transparent Cl-doped ZnO thin films via aerosol-assisted chemical vapour deposition," *Journal of Materials Chemistry A,* vol. 6, no. 26, pp. 12682-12692, 2018.

Figures caption list

Figure 1. X-ray diffraction patterns of undoped and Cl-doped Fe_2O_3 samples. Indexed peaks correspond to hematite (JCPDS 24-0072); * indicates maghemite, observed only in FeCl-0.18.

Figure 2. DRIFTS spectra of undoped and Cl-doped Fe_2O_3 before and after lixiviation: (a) Fe_2O_3, (b) FeCl-0.18, (c) FeCl-0.23.

Figure 3. TEM and high-resolution TEM (HRTEM) micrographs of Fe_2O_3, FeCl-0.23, and lixiviated FeCl-0.23. (a,c,e) Low-magnification TEM (scale bar: 100 nm) showing particle aggregates; yellow labels indicate apparent particle diameters. (b,d,f) HRTEM (scale bar: 10 nm) with lattice fringes indexed to hematite, $d_{012} \approx 0.367$ nm (JCPDS 24-0072). Panels correspond to: (a,b) Fe_2O_3, (c,d) FeCl-0.23, (e,f) FeCl-0.23 lixiviated.

Figure 4. UV–Vis diffuse reflectance spectra of undoped and Cl-doped Fe_2O_3.

Figure 5. Tauc plots used to determine the optical band gap (E_g) of undoped and Cl-doped Fe_2O_3 samples: (a) Fe_2O_3, (b) FeCl-0.03, (c) FeCl-0.04, (d) FeCl-0.05, (e) FeCl-0.18, and (f) FeCl-0.23.

Figure 6. Color difference ΔE*ab (CIE76) for undoped and Cl-doped Fe_2O_3 as a function of retained Cl^- content (XRF, mol%). ΔE was computed with respect to the undoped sample under the same conditions (nonlixiviated or lixiviated).

Figure 7. Nyquist impedance plots ($-Z''$ vs Z') of undoped and Cl-doped Fe_2O_3 pellets measured at room temperature: (a) nonlixiviated, (b) lixiviated. Symbols are experimental data and solid lines are the best fits to the equivalent circuit shown in the inset (series of two R-CPE elements). Z' and $-Z''$ are expressed in MΩ·m.

Figure 8. (a) Electrical conductivity, σ, versus retained Cl^- content (XRF, mol%) for nonlixiviated and lixiviated pellets (room temperature). (b) Relative increase with respect to the undoped sample: measured σ (black squares) and carrier-count model N (red circles; one electron per Cl^-).

Figure 1S. Colorimetric parameters a* (a), b* (b), and L* (c) of undoped Fe_2O_3 and Cl-doped Fe_2O_3 lixiviated and non-lixiviated samples.

Tables caption list

Table 1. Lattice parameters and crystallite sizes of undoped and Cl-doped Fe_2O_3, and phase fractions obtained from Rietveld refinement. Values in parentheses are estimated standard deviations in the last digit. “FeCl-x” denotes the measured Cl content (mol%). Maghemite was detected only for FeCl-018.

Table 2. Density, specific surface area (SSA), total specific surface area (TSA), specific grain-boundary area (SGB), and SGB/SSA ratio for undoped and Cl-doped Fe_2O_3 (FeCl-x). Values are reported as mean ± standard uncertainty.

Table 3. Interfacial excess of Cl^- at the surface (Γ_S) and at the grain boundaries (Γ_{gb}) for undoped and Cl-doped Fe_2O_3 (FeCl-x) samples. Values are in $\mu mol/m^2$ and are reported as mean ± standard uncertainty. excesses Γ_S is normalized by SSA; Γ_{gb} is normalized by SGB (see Eqs. (3)-(4) and (6)).

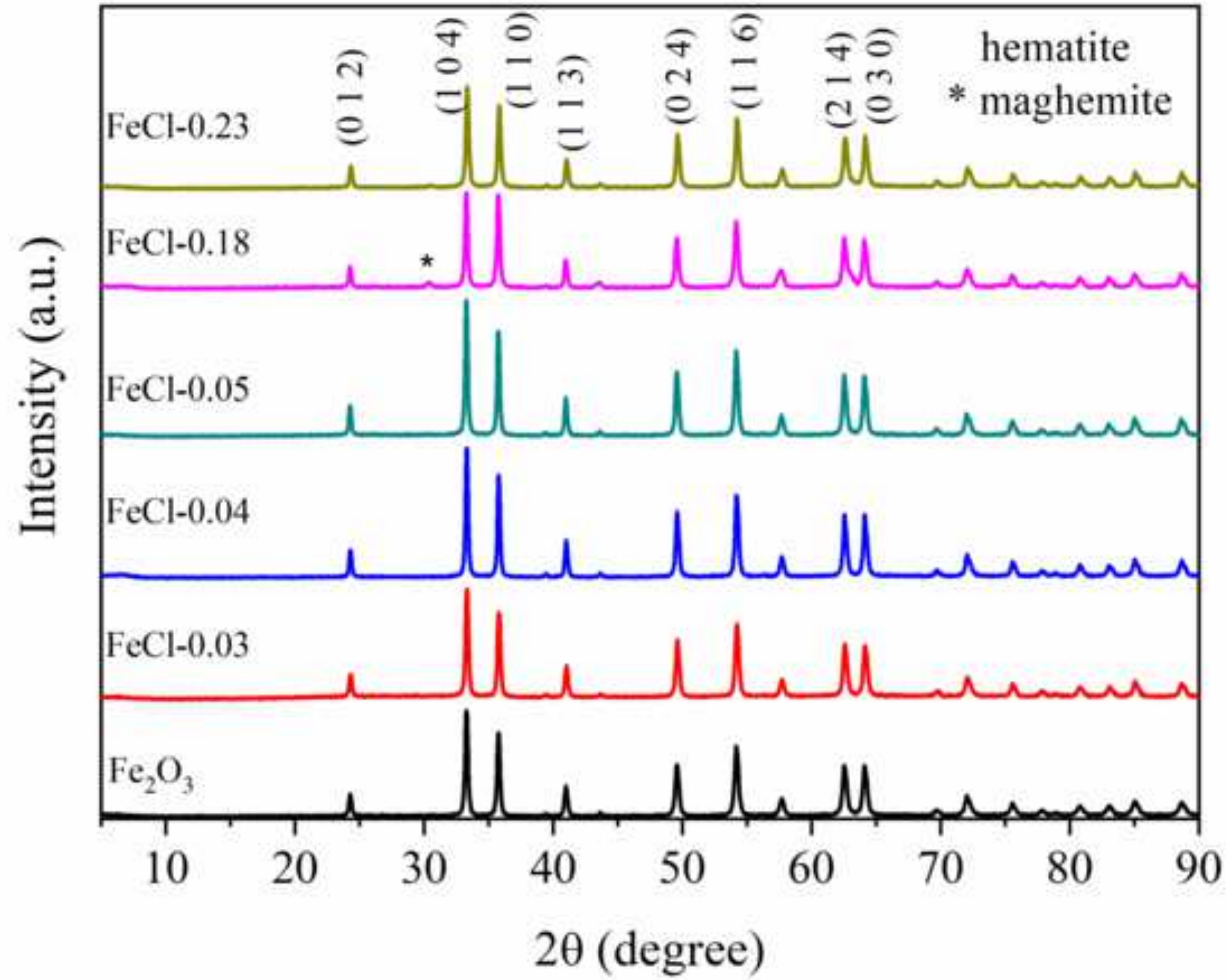
hematite
* maghemite
(0 1 2)
(1 0 4)
(1 1 0)
(1 1 3)
(0 2 4)
(1 1 6)
(2 1 4)
(0 3 0)
FeCl-0.23
FeCl-0.18
*
FeCl-0.05
FeCl-0.04
FeCl-0.03
Fe_2O_3
Intensity (a.u.)
10
20
30
40
50
60
70
80
90
2θ (degree)

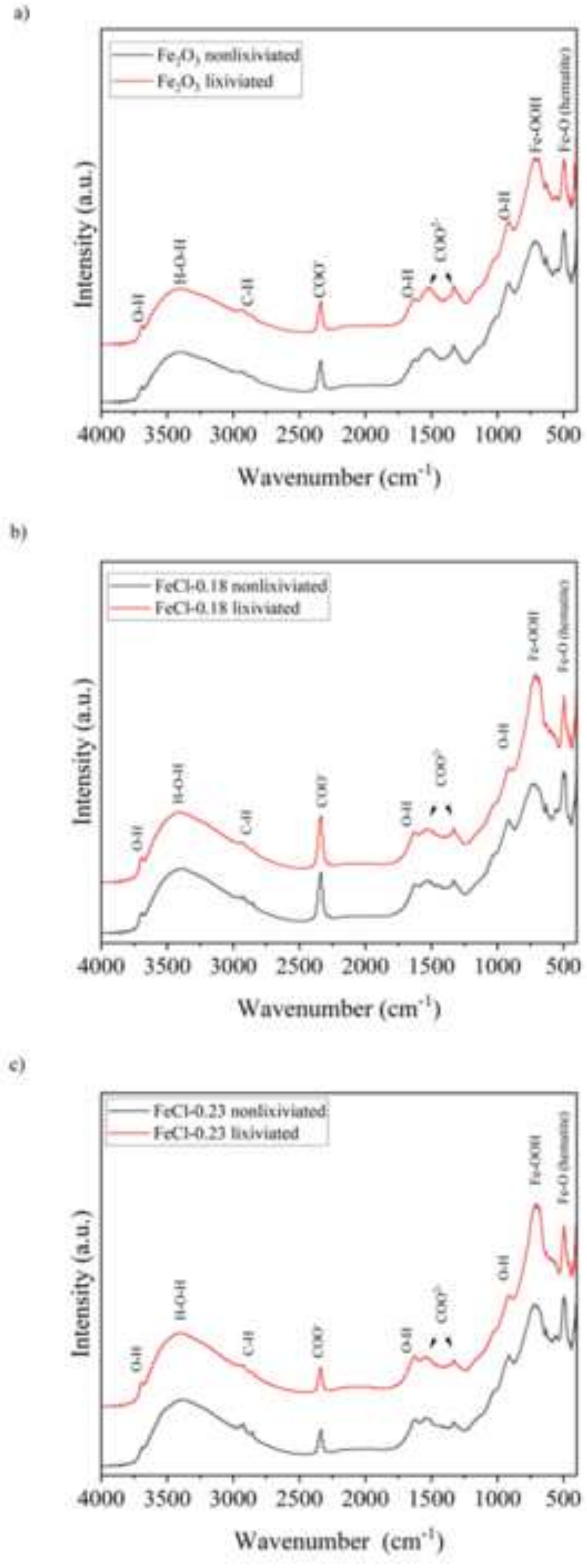
a)
Fe₂O₃ nonlixiviated
Fe₂O₃ lixiviated
Intensity (a.u.)
O-H
H-O-H
C-H
COO⁻
O-H
COO²⁻
O-H
Fe-OOH
Fe-O (hematite)
4000
3500
3000
2500
2000
1500
1000
500
Wavenumber (cm⁻¹)
b)
FeCl-0.18 nonlixiviated
FeCl-0.18 lixiviated
Intensity (a.u.)
O-H
H-O-H
C-H
COO⁻
O-H
COO²⁻
O-H
Fe-OOH
Fe-O (hematite)
4000
3500
3000
2500
2000
1500
1000
500
Wavenumber (cm⁻¹)
c)
FeCl-0.23 nonlixiviated
FeCl-0.23 lixiviated
Intensity (a.u.)
O-H
H-O-H
C-H
COO⁻
O-H
COO²⁻
O-H
Fe-OOH
Fe-O (hematite)
4000
3500
3000
2500
2000
1500
1000
500
Wavenumber (cm⁻¹)

Figure 3

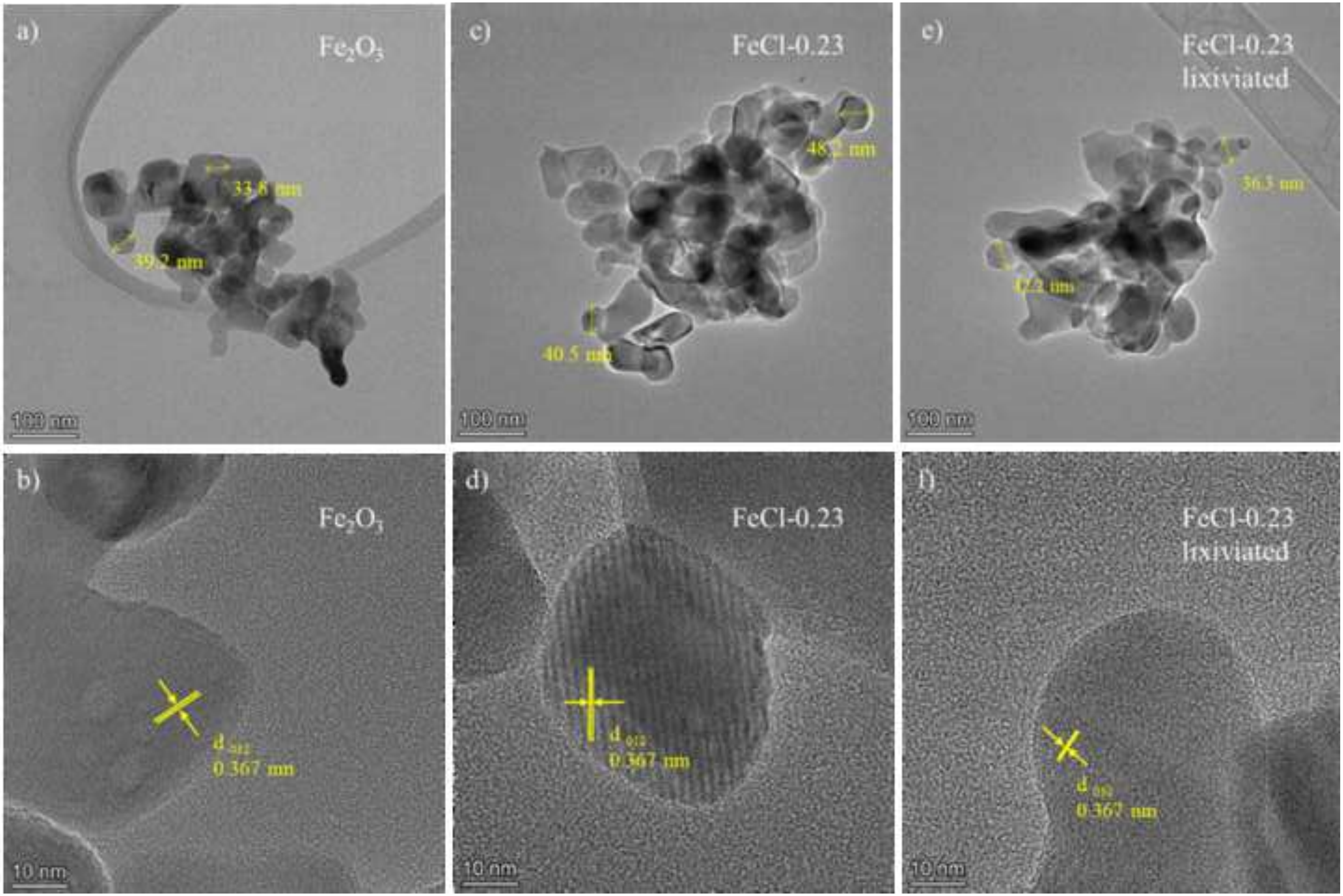
a)
Fe_2O_3
33.8 nm
39.2 nm
100 nm
c)
FeCl-0.23
48.2 nm
40.5 nm
100 nm
e)
FeCl-0.23
lixiviated
36.3 nm
100 nm
b)
Fe_2O_3
d_{012}
0.367 nm
10 nm
d)
FeCl-0.23
d_{012}
0.367 nm
10 nm
f)
FeCl-0.23
lixiviated
d_{012}
0.367 nm
10 nm

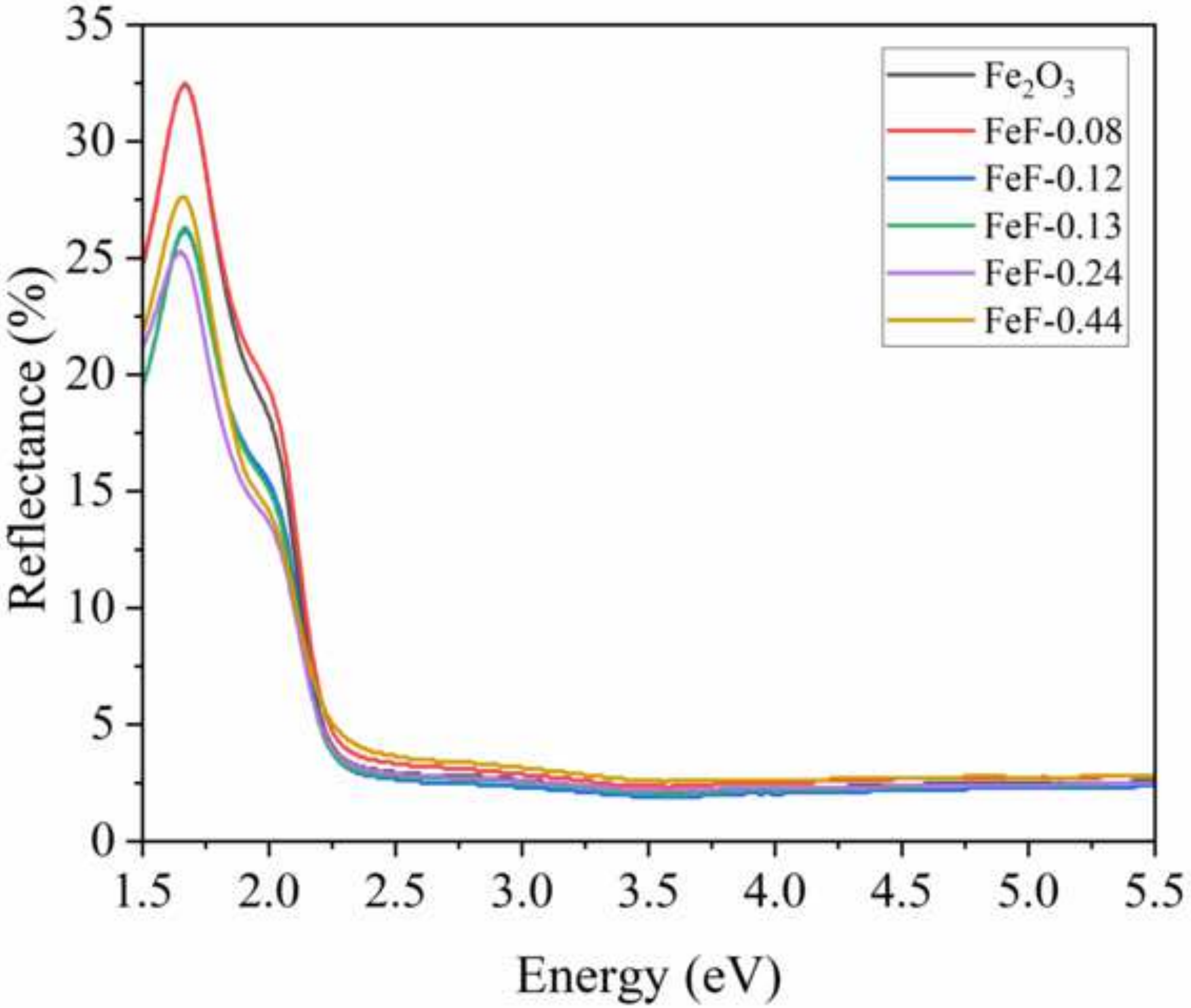
Reflectance (%)
Energy (eV)
0
5
10
15
20
25
30
35
1.5
2.0
2.5
3.0
3.5
4.0
4.5
5.0
5.5
Fe_2O_3
FeF-0.08
FeF-0.12
FeF-0.13
FeF-0.24
FeF-0.44

Figure 5

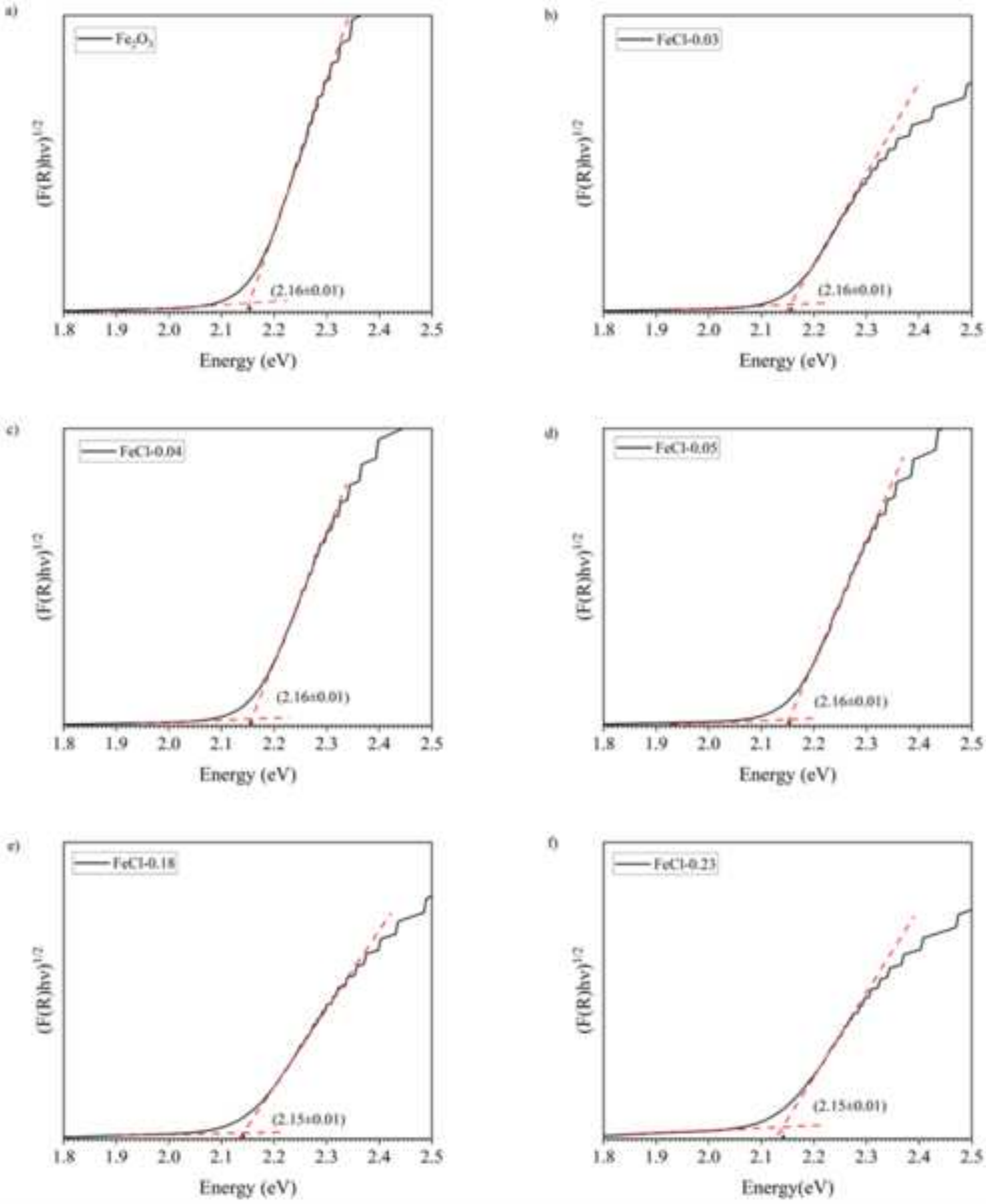

a)
Fe$_2$O$_3$
(2.16±0.01)
b)
FeCl-0.03
(2.16±0.01)
c)
FeCl-0.04
(2.16±0.01)
d)
FeCl-0.05
(2.16±0.01)
e)
FeCl-0.18
(2.15±0.01)
f)
FeCl-0.23
(2.15±0.01)
(F(R)hv)$^{1/2}$
Energy (eV)
Energy(eV)
1.8
1.9
2.0
2.1
2.2
2.3
2.4
2.5

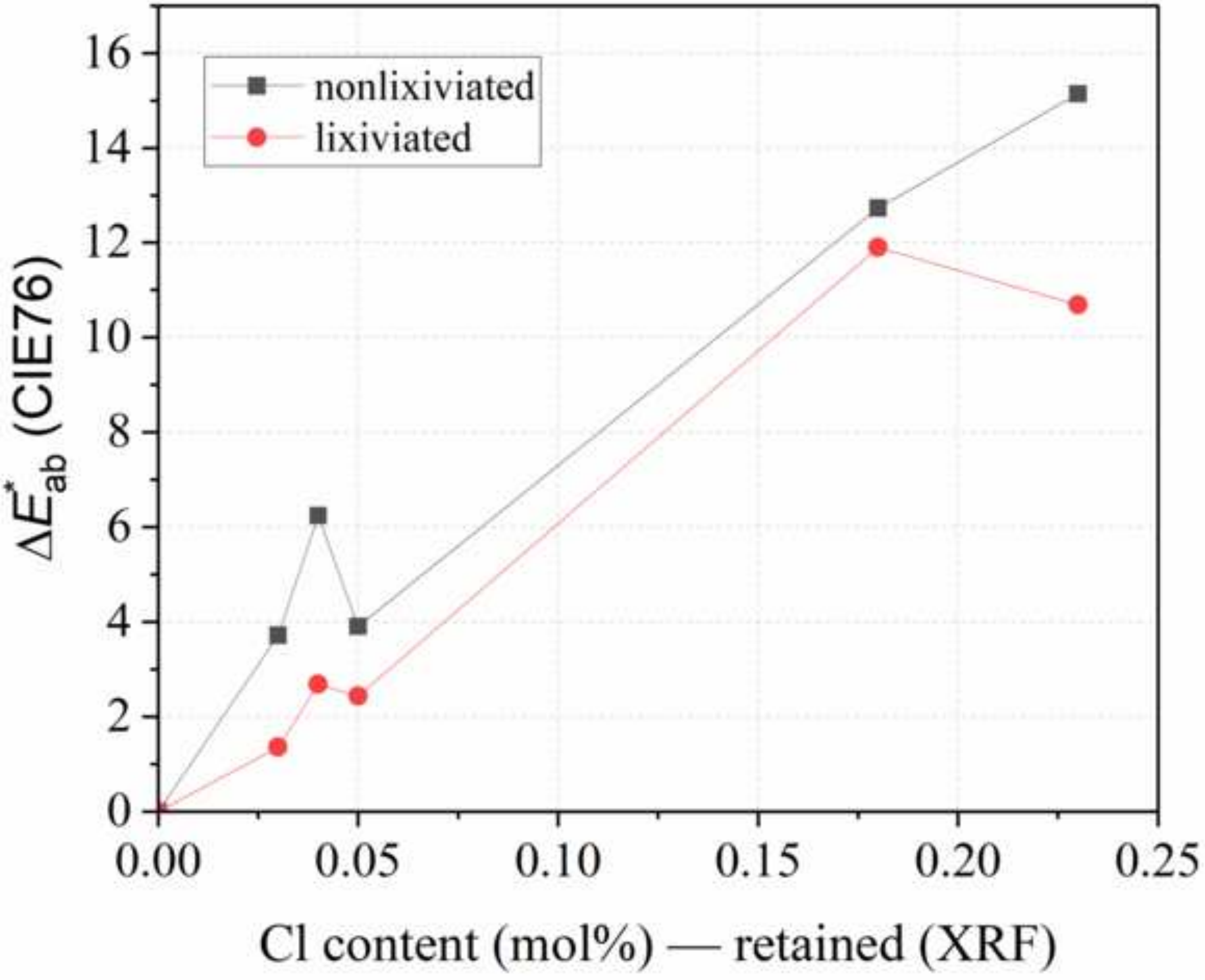

ΔE^*_{ab} (CIE76)
16
14
12
10
8
6
4
2
0
0.00
0.05
0.10
0.15
0.20
0.25
Cl content (mol%) — retained (XRF)
nonlixiviated
lixiviated

Figure 7

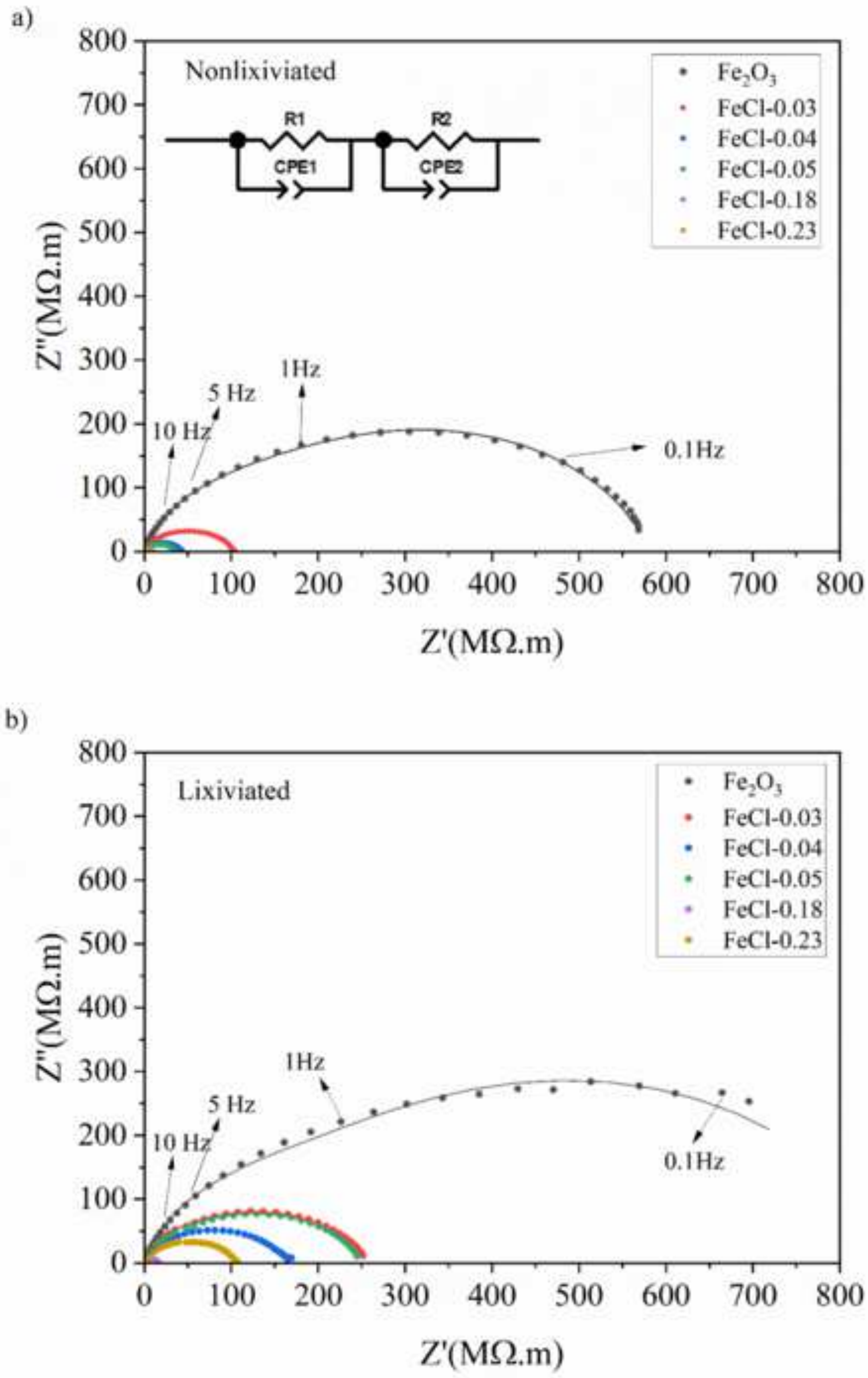
a)
Nonlixiviated
R1
R2
CPE1
CPE2
Fe_2O_3
FeCl-0.03
FeCl-0.04
FeCl-0.05
FeCl-0.18
FeCl-0.23
1Hz
5 Hz
10 Hz
0.1Hz
Z''(MΩ.m)
Z'(MΩ.m)
0
100
200
300
400
500
600
700
800
b)
Lixiviated
Fe_2O_3
FeCl-0.03
FeCl-0.04
FeCl-0.05
FeCl-0.18
FeCl-0.23
1Hz
5 Hz
10 Hz
0.1Hz
Z''(MΩ.m)
Z'(MΩ.m)

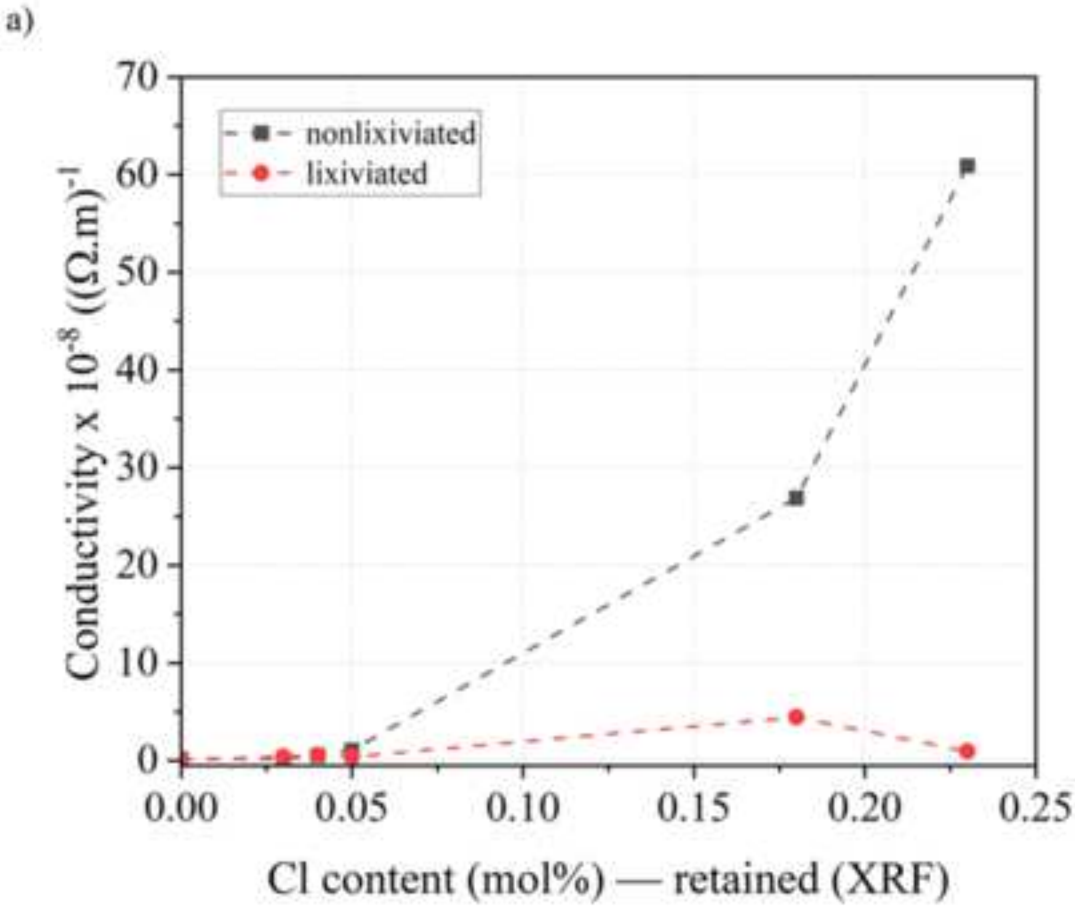
a)
Conductivity x 10^{-8} ((Ω.m)$^{-1}$
Cl content (mol%) — retained (XRF)
nonlixiviated
lixiviated
0
10
20
30
40
50
60
70
0.00
0.05
0.10
0.15
0.20
0.25

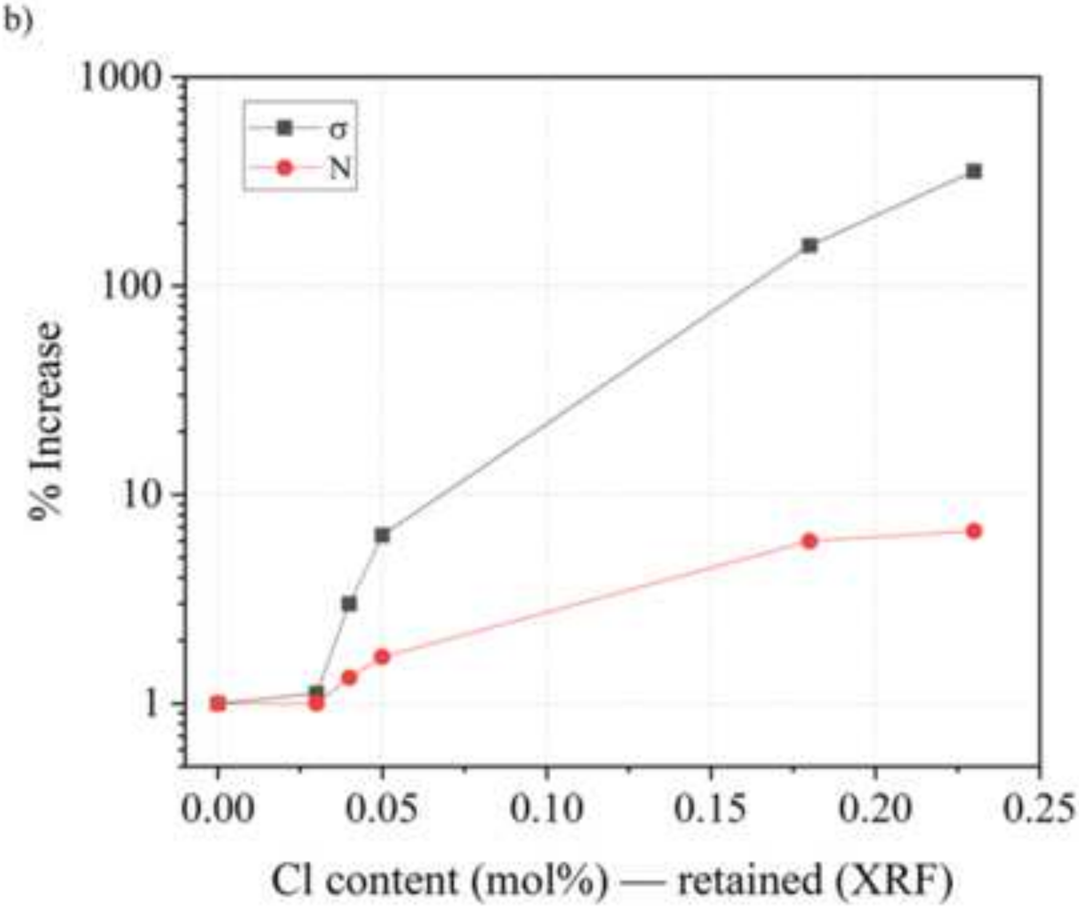
b)
% Increase
Cl content (mol%) — retained (XRF)
σ
N
1
10
100
1000
0.00
0.05
0.10
0.15
0.20
0.25